Semnan University

Journal of Modeling & Simulation in Electrical & Electronics Engineering (MSEEE)

Journal homepage: **https://mseee.semnan.ac.ir/**

ISSN: 2821-0786

High-Fidelity Optical CNOT Gates Enabled by Rydberg-Mediated Phase Control

Ali Farmani [1*] and Anis Omidniaee[2]

***Abstract*- In this paper, we first design a photonic crystal laser chamber based on indium phosphide gallium arsenide and zinc oxide quantum dots due to the large energy gap of about 3.37 eV for laser beam propagation in terahertz applications. ZnO is easily grown in the form of nanorods, nanowires, and thin films and therefore can perform well in confined modes of photonic crystals. The results are obtained by examining the quality factor criteria of the dispersion temperature effect and the constant radius to lattice ratio to enhance spontaneous emission for improving optical pumping. In these materials, the quality factors for indium arsenide and aluminum oxide are 227.98 and 131.95, respectively, for the hybrid gain medium including gallium arsenide, aluminum oxide, and zinc oxide. Finally, the photonic crystal laser beam is driven to quantum logic gates resulting in angle and rotation changes, and its probability function for quantum laser application are measured.**

Keywords: photonic crystal, quantum dots, gain medium, CNOT gate, Quantum Laser

I. INTRODUCTION

Due to their robust optical confinement and ease of transfer to non-native substrates, membrane photonic devices have garnered considerable scholarly attention [1]-[2]. The repositioning of electrodes to the device's lateral side [3] presents novel challenges in carrier injection technology, primarily because the membrane cladding layers are frequently composed of air or insulating materials. Carrier injection can transpire through two mechanisms: via a lateral pin junction, wherein the active material remains unaltered, or through a conventional vertical pin junction established during the epitaxial growth of the membrane [4]. Lateral doping, which is a regrowth technique, offers greater flexibility as the doping regions are localized and planar processing is maintained. When integrated with lateral injection and an embedded heterogeneous active region, it demonstrates enhanced efficiency. By creating a large-area standing wave coupled with light extraction in the vertical direction via first-order diffraction, the lateral coupling of light amplification and band-edge lasing is realized. The far-field pattern exhibits minimal divergence due to the extensive coherent resonance. In confined-mode nanolasers, the lasing threshold of colloidal quantum dots, when utilized alongside silicon nitride-based photonic crystals, can be as low as 10.5 kW/cm². This nanolaser features a square lattice arrangement composed of cylindrical air holes within a dielectric plate having a refractive index of 10, with quantum dots embedded within. The power density is quantified at 5 kW/cm². An even surface topography is paramount for effectively removing excess quantum dots from the surface in the confined state, ensuring complete filling of the air voids, and achieving a high quality factor alongside a low lasing threshold [5]-[7]. The photonic crystal nanocavity is fabricated by superimposing two photonic crystal structures at a designated rotation angle, resulting in an exceptionally high quality factor and significant light confinement within an extremely compact mode volume. In a twisted cavity, the resonance wavelength and optical mode distribution can be dynamically modified at the nanoscale through the random selection of the twist angle. These semiconductor nanolasers employ multiple quantum wells of indium gallium arsenide phosphide as the gain medium and demonstrate low lasing thresholds within the C-band. With a minimal area of approximately 25 μm² and a theoretical mode volume (Vm) of about 0.47 $(\lambda/n)^3$, large-angle (5°) twisted photonic crystal nanolasers are optically pumped at ambient temperature, yielding single-mode emission with an extraordinarily low lasing threshold of approximately 1.25 kW/cm². Photonic crystal nanocavity lasers emit a continuous wave at a wavelength of 1540 nm, characterized by an extremely low threshold current of 10.2 μA. Indium phosphide-based photonic crystal lasers exhibit this threshold current of 10.2 μA [8]. The lateral pumping configuration of photonic crystal nanolasers experiences

Received; 2025-10-31 Revised; 2025-12-06 Accepted; 2025-12-27

[1] Department of Nanoelectronics Engineering, Lorestan University, Khoramabad, Iran.
[2] Department of Nanoelectronics Engineering, Lorestan University, Khoramabad, Iran
*Corresponding author: Farmani.a@lu.ac.ir

Cite this article as:
Farmani, A. and Omidniaee, A. (2025). High-Fidelity Optical CNOT Gates Enabled by Rydberg-Mediated Phase Control. *Journal of Modeling & Simulation in Electrical & Electronics Engineering (MSEEE).* Semnan University Press . *5 (4),* 45-57.
DOI: https://doi.org/ https:/ 10.22075/MSEEE.2025.39558.1237

significant carrier leakage, which arises from unintended spontaneous emission at the pi interface, thus limiting the injection efficiency to a mere 3%, with a further decrease in efficiency observed at higher currents. Consequently, researchers have shifted their focus to the thermal stability of quantum dot materials derived from indium phosphide and aluminum gallium arsenide. The high density of the indium phosphide/aluminum gallium arsenide mixture enables accurate (001) orientation on gallium arsenide substrates; however, it necessitates relatively low substrate temperatures. [9]-[10]. However, indium phosphide/gallium arsenide quantum dot materials primarily have issues pertaining to material properties and growth dynamics. The relatively modest lattice mismatch of around 3. 2% in ArsinGaLiM, as opposed to around 7. 2%, reduces the strain energy during the StranskyKrastunov growth, which widens the size distribution of quantum dots. The presence of this inhomogeneity requires meticulous optimization of the growth process to achieve uniform and high-quality quantum dots. This is achieved by adjusting the layer thickness during the development of quantum dots in molecular beam epitaxy, utilizing a blend of indium phosphide and gallium arsenide deposition thickness, along with an altered indium alignment method in L and C-band quantum dot lasers. This approach leads to a low threshold current density of 21. 35 kA/cm[11]. The lower optical loss in the photonic crystal surfaceemitting laser designs with horizontal resonance and vertical emission in indium phosphide and gallium arsenide quantum dots, which have a larger singlemode area, enables highpower, singlemode operation and very low divergence angle. To lower the threshold current to 80 mA, these nanolasers were created by implanting protons in the pcladding layer. The laser wavelength is clearly dependent on the lattice constant, with each 5 nm increase in the lattice constant resulting in a 15 nm increase in the laser wavelength. The buried secondary epitaxial structure has shown exceptional performance, primarily due to the fact that the layer is close to the active region, which greatly enhances the optical confinement factor and improves the total device performance by increasing the optical feedback. The substrateside emission configuration allows for the pside connection to the heat sink, therefore increasing thermal dissipation and enhancing the overall device performance. These discoveries offer useful guidance for the creation and optimization of highperformance 1. 3 m gallium arsenidebased surfaceemitting lasers [12]. Colloidal leadchalcogenide materials were regarded in quantum dot nanolasers. However, the exciton population was wiped out by high nonradiative Auger recombination caused by trap states, which degraded the light amplification and led to high gain thresholds. A binary mixture of colloidal lead quantum dots and zinc oxide nanocrystals was used to deactivate the trap states inside the sodium diethyl dithiophosphate gain medium. In addition, the transient absorption method reveals a fivefold enhancement in the Auger lifetime, indicating a reduction in trap-assisted Auger recombination. Consequently, the threshold for enhanced spontaneous emission at 1650 nm, with a linewidth of 1.23 nm, was halved. Despite this, these colloidal quantum dot nanolasers manage to achieve both stability and a high integration density at the same time. Research indicates that employing colloidal quantum dots with zinc selenide/cadmium selenide core-shell structures in a surface-based integrated circular Bragg resonator can result in a mode confinement factor approaching unity at 89% and a Purcell coefficient reaching as high as 22.7. This configuration also offers a significant confinement factor and a low laser threshold of 17 μJ/cm², which is 70% less than the threshold of 56 μJ/cm² observed in surface-emitting lasers with vertical cavity colloidal quantum dots [13]-[16]. Due to the self-assembled nature of StranskyKrastanov growth, conventional quantum dots encounter substantial difficulties in epitaxially controlling their spectral inhomogeneity and spatial nucleation position. In nanocavities integrated with small mode volumes, the cavity enhancement caused by the Purcell effect is weak in the coupling regime, even though thermal control and surface defect states continue to affect the high photon extraction efficiency of 85% in a circular Bragg grating resonator [17]. Buried photonic defects, which need little etching, may help microcavities made of these solve these issues. Selfassembly during epitaxial development results in their formation; their location is controlled at the quantum dot under a buried stress; hence, postgrowth lithography is not necessary [18]. Furthermore, the transient absorption technique demonstrates a fivefold increase in the Auger lifetime, suggesting a decrease in trap-assisted Auger recombination. As a result, the threshold for enhanced spontaneous emission at 1650 nm, which has a linewidth of 1. 23 nm, has been reduced by half. Nonetheless, these colloidal quantum dot nanolasers successfully combine stability with a high integration density. Studies show that using colloidal quantum dots with zinc selenide/cadmium selenide core-shell structures in a surface-mounted integrated circular Bragg resonator can achieve a mode confinement factor almost reaching unity at 89% and a Purcell coefficient as high as 22. 7. This setup also provides a notable confinement factor along with a low laser threshold of 17 μJ/cm², significantly lower than the 56 μJ/cm² threshold found in vertical cavity colloidal quantum dots from surface-emitting lasers. Additionally, selenide phosphide quantum dots display nonlinear features, including a modulation depth of 8. Additionally, selenide phosphide quantum dots display nonlinear features, including a modulation depth of 8.8% [19] .The output power from these nanolasers reached 7 W, and they exhibited a brightness level of 180 mW/cm²/s. However, during their development, particularly in structures made of gallium arsenide with certain structural constraints, a suspended bilayer torsional design linked to quantum dots in the near-infrared can easily be affected. Additionally, the mode field of the nanocavity primarily exists within the air gaps, which limits the effective interaction between the quantum dot and the cavity due to inadequate spatial overlap. Recently, researchers have been examining how a Moiré nanocavity interacts with a single quantum dot. Moiré nanocavities are created by the interaction of two identical photonic graphene layers that are twisted at a specific angle. When the Bloch modes of these layers couple, flat bands appear in the energy spectrum. These flat bands allow for light trapping that is not reliant on the momentum of the Bloch wave, leading to modes that have a group velocity of zero [20].

II. DESIGN AND STRUCTURE

A photonic crystal-based nanolaser was developed

utilizing the finite difference time domain numerical solution method. This design incorporated a hybrid gain medium consisting of a 10 nm thick layer of aluminum dioxide, which has a refractive index of 1. 75, alongside a gallium arsenide oxide dielectric layer. The primary objective of this configuration was to enhance optical pumping. This structure, as seen in Figure 1, The photonic crystal profiles in the symmetric A-state and the antisymmetric B-state are shown in Figure .is made up of a silicon substrate with a 40 nm thick aluminum gallium arsenide layer in the middle, and a gallium arsenide waveguide layer is formed on top of it with a 170 nm thickness, which is situated between two 40 nm thick aluminum gallium arsenide layers and two 5 nm thick gallium a layers, respectively. The membrane of the photonic crystal consists of a triangular lattice featuring air holes, with a lattice pitch, denoted as 'a', measuring 366 nm. In this context, a hole radius of 135. 4 nm, equivalent to 0. 37a, is considered. Photonic crystal nanolasers, which utilize thin semiconductor films in conjunction with single indium phosphide quantum dots, are particularly noteworthy due to their minuscule volume and ability to manipulate the magnetic field within the cavity, facilitating atom emission. This capability allows for the design of polarization-related patterns. The incorporation of silicon in these structures is advantageous due to its low cost, high integration potential, and compatibility with integrated circuit manufacturing processes. However, the optical pumping efficiency of these devices is constrained when paired with gallium arsenide and aluminum gallium arsenide materials. Research indicates that zinc oxide is a promising alternative, as it possesses a relatively high exciton binding energy of approximately 60 meV, which exceeds that of other materials [21].

$$n\_ave=\sqrt{(〖n^2〗\_b\ (1-FF)+〖n\_h〗^2\cdot FF)} \quad (1)$$

The refractive index of the collision zone and air is represented by n_b 〖 and n〗_h in this relationship.

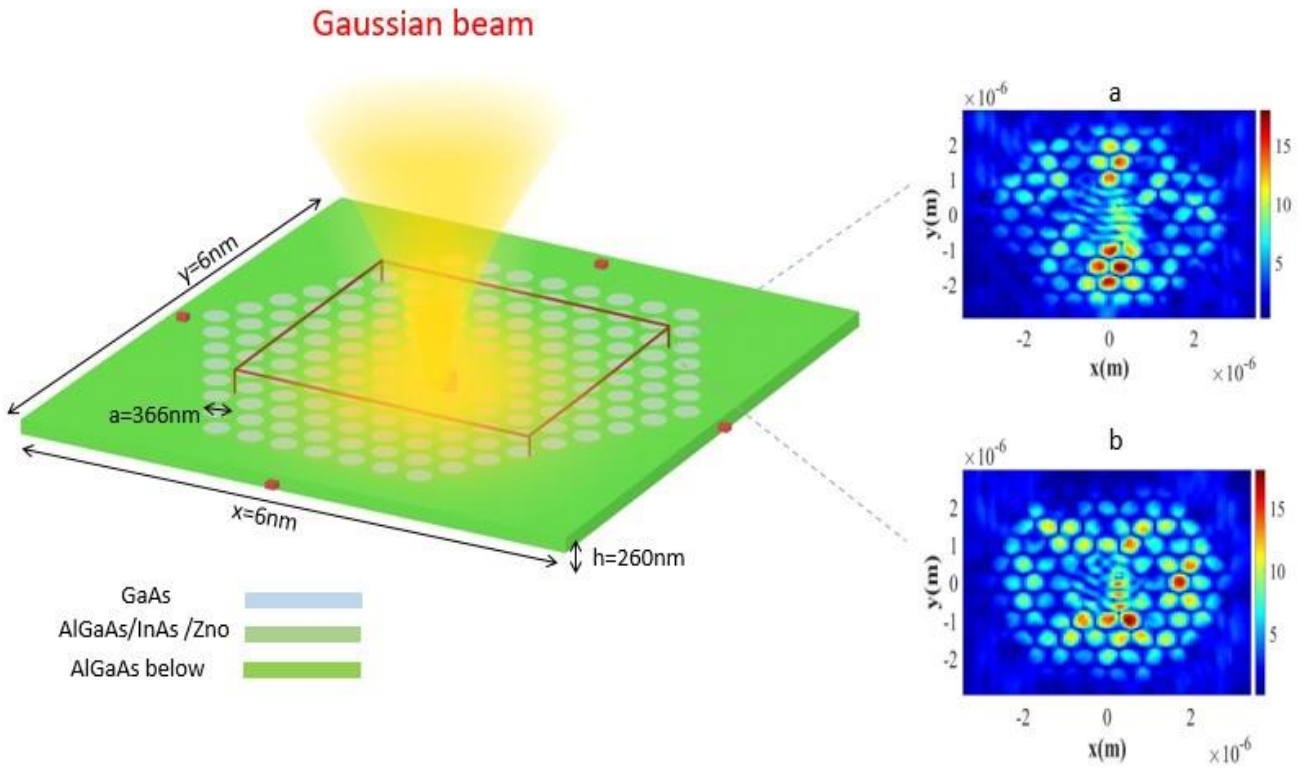

Fig 1: Three-dimensional perspective of the photonic crystal nanolaser architecture.

III. METHODS SECTION

In this work, we evaluate eight phase-shifting configurations, each defined by a unique combination of phase-step sequencing and modulation pattern. These configurations differ in their noise susceptibility, robustness to phase-step miscalibration, and sensitivity to harmonic distortions. Assessing all eight variants enables a systematic optimization of the reconstruction strategy and ensures that the selected configuration maximizes stability and accuracy under practical measurement conditions.

Step-by-Step Proposal of the Idea

Step 1: Selecting the Materials and Gain Media
The study begins by choosing suitable materials for the photonic crystal laser cavity: indium phosphide (InP), gallium arsenide (GaAs), aluminum oxide (Al_2O_3), and zinc oxide (ZnO) quantum dots. The rationale is based on their large energy gaps (~3.37 eV for ZnO), which make them appropriate for terahertz laser propagation and efficient optical pumping. ZnO is highlighted because it can be easily grown in nanorods, nanowires, or thin films,

which helps achieve strong mode confinement in the photonic crystal cavity.

Step 2: Designing the Photonic Crystal Laser Cavity
A photonic crystal laser chamber is designed using these materials. The design considers dispersion effects, temperature dependence, and geometrical parameters such as the constant radius-to-lattice ratio to optimize the laser properties. The goal is to enhance spontaneous emission and overall optical pumping efficiency.

Step 3: Calculating Performance Metrics
The quality factor (Q-factor) of the cavity is evaluated to quantify performance. These calculations confirm that the cavity design supports efficient lasing and strong light-matter interaction.

Step 4: Application to Quantum Logic Gates
After optimizing the photonic crystal laser, it is applied to quantum logic gates. The study measures how the laser's angle, rotation, and probability function change in this context. This demonstrates the potential of the designed system for quantum laser applications, bridging photonic crystal laser technology with quantum information processing.

Step 5: Highlighting Novelty and Utility
The novelty lies in combining:
Hybrid gain media with high-Q factors. Nanostructured ZnO for strong confinement. Integration with quantum logic gates, showing practical quantum photonic applications.

IV.RESULTS AND DISCUSSIONS

The Gaussian emission spectrum is initially found at 1210 nm and 1110 nm, respectively, in the quantum dots' recombination of the ground state and first excited electron-hole pairs. The variation in size of the self-assembled quantum dots is shown by the width of each band. The hole emission spectrum, in contrast to the wide emission bands of the quantum dot array, displays distinct lines that span the spontaneous quantum dot emission band as the ratio of the nanohole radius to the lattice constant rises. The quality factor of the hole restricts the linewidth of the modes, which increases with the quality factor ratio of 131. 95. As shown in Figure 2, the mode intensity increases as the cavity modes enter into resonance with the majority of the quantum dots, i. e. , near the peak position of the quasiGaussian band.

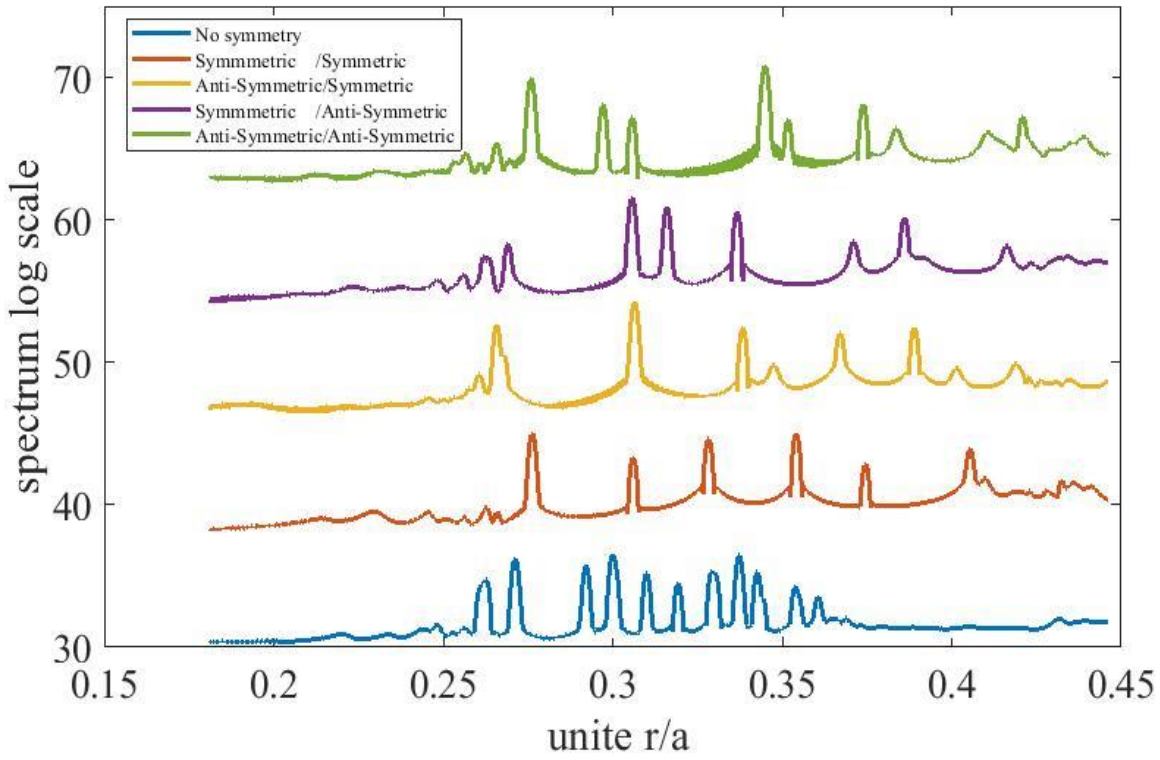

Fig 2: The Gaussian emission spectrum plot as a function of radius to lattice constant.

To enhance optical pumping within a waveguide made of aluminum gallium arsenide, quantum dots are positioned in the gallium interlayer. Additionally, aluminum oxide functions as a dielectric layer with a refractive index of 1. 75, serving as a low refractive index material to confine the field for the gain medium.

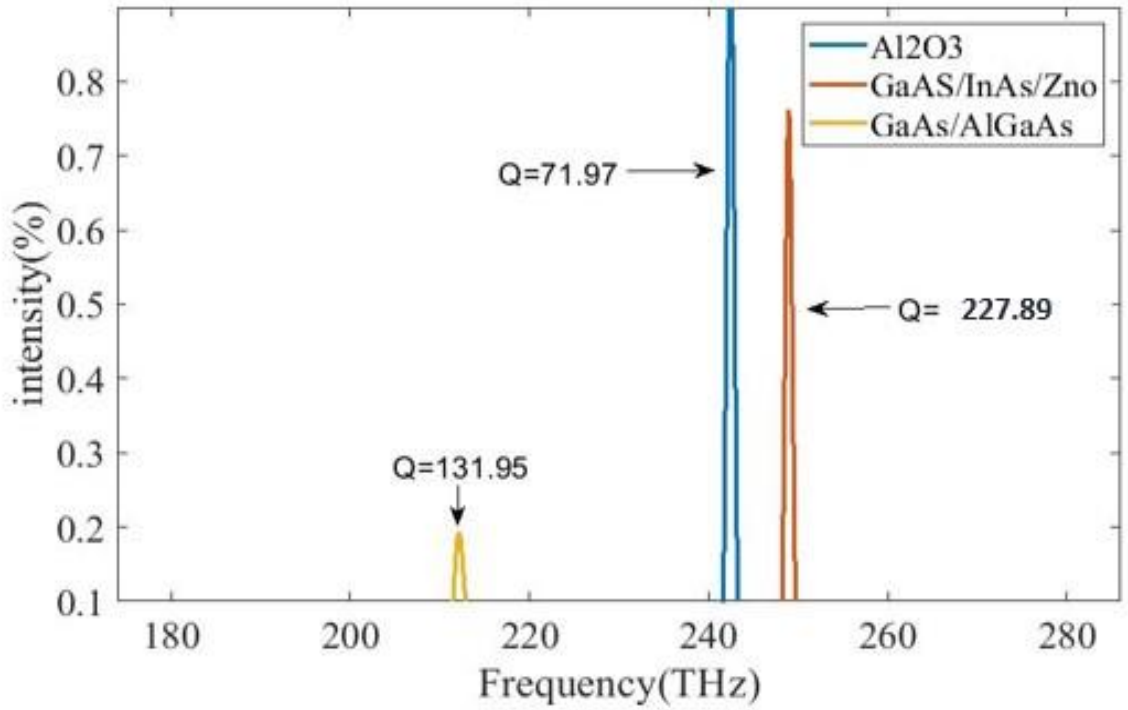

Figure 3: The emission intensity as a function of frequency, spanning from 180 to 280 terahertz, within a hybrid gain medium.

As shown in Figure 4, the gallium arsenate gain material has a high refractive index of 3. 4. The effect of indium arsenic zinc oxide and gallium arsenate in increasing the confinement intensity of the gain medium is also determined by their quality factor in Figure 5, which is maximized at a frequency of 212 THz.

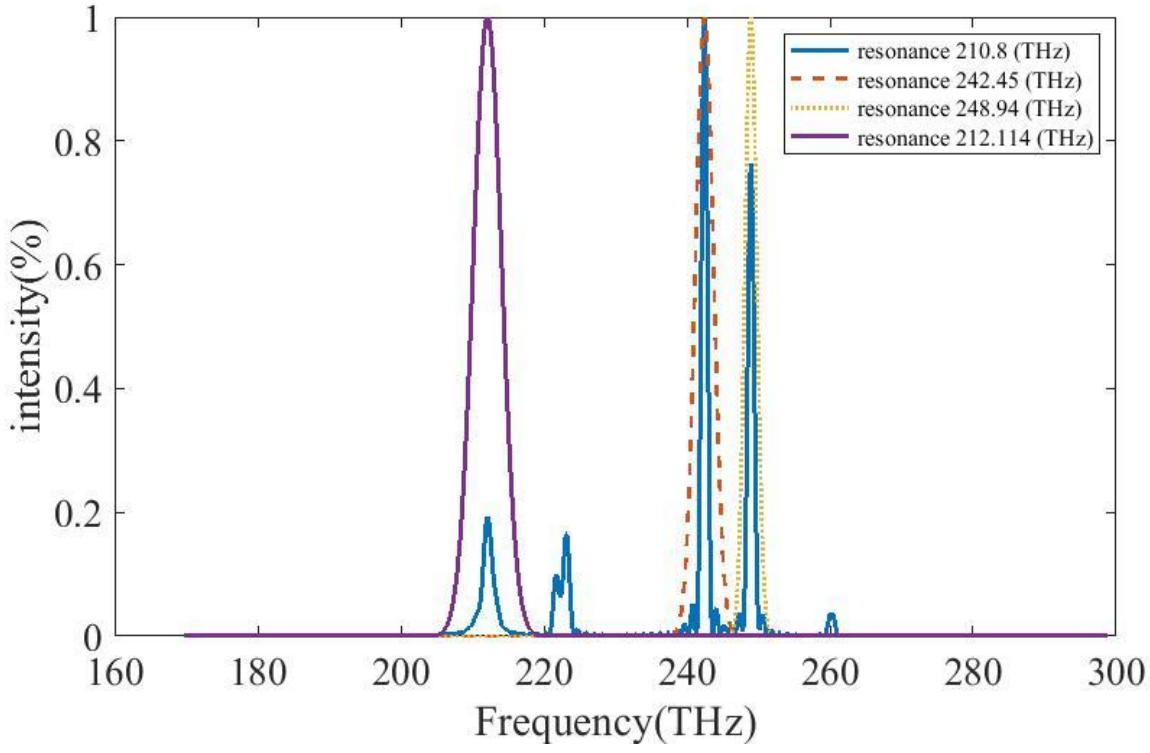

Figure 4: Emission intensity vs. frequency in the range of 180 to 280 terahertz.

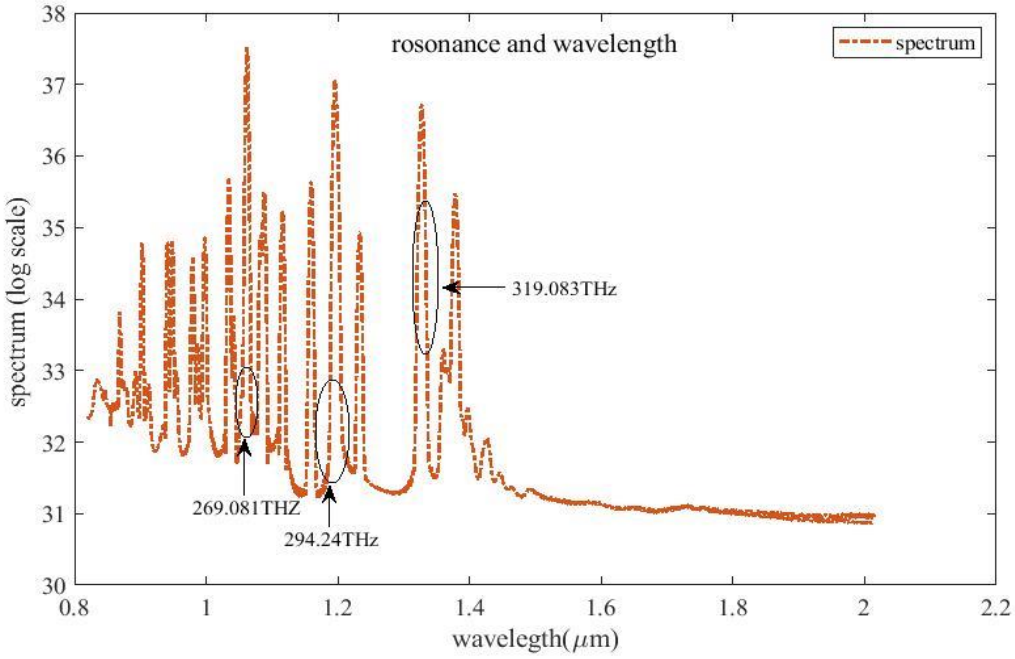

Fig 5: The Euler spectrum, which peaks at 212 terahertz, is shown in the graph.

The only well-defined current injection window identified is region I, as illustrated in Figure 5. The figure displays the curves for quantum dots with lattice constants of 366nm, along with injection apertures of 60 μm and 40 μm at a temperature of 10°C. In Fig. 6, the parameter is presented. The current confinement provided by the gallium arsenide and zinc oxide layers leads to a decrease in the threshold current by around 0. 25 mA, even though there is an increase in the threshold current density. The device with a 0.1-micrometer injection aperture did not exhibit a reduction in threshold current. The observed increase in threshold current density is linked to the discrepancy between the gain spectra and the limitations set by the photonic crystals. Furthermore, the current density tends to rise with increasing temperature.

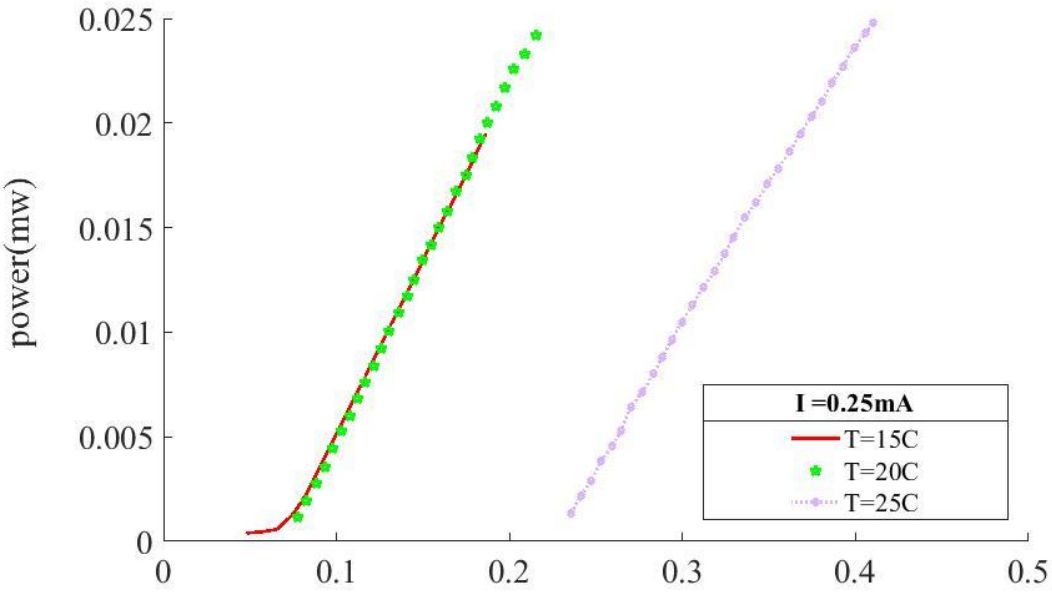

Figure 6: The output gain curve of a photonic crystal laser with current excitation in a gallium arsenic and zinc oxide gain environment as a function of temperature fluctuations.

Absorption is one of the most important factors determining the threshold, efficiency, linewidth, and output stability. Because nanolasers have very small dimensions, even a small amount of absorption can significantly change the optical and quantum behavior of the laser. Increasing absorption in the active material reduces the Q-factor, which in turn increases the optical pumping threshold. The effect of material absorption is

examined in Figure 6. The results show that the use of the aluminum gallium arsenic/gallium arsenic material combination shows a lower absorption of 70% compared to the gallium arsenic/indium arsenic/zinc oxide material combination. In a similar vein, the indium arsenide quantum dot material's absorption impact has been examined in isolation throughout the wavelength range of 0.5 to 1600 nm. The quality was evaluated by measuring the absorption at 1000 nm, yielding a result of 0.8%, as demonstrated in Figure 6. The amount of light trapped in this area is estimated to be 1455.3 times the factor. The variations in the gain environment are depicted in Figure 7. Zinc oxide, indium arsenic, and aluminum dioxide coatings have all been examined. The aluminum dioxide layer has a lower peak than the variations in time with the field intensity, and it is nearly identical for all of them: the indium, arsenic, and zinc oxide layers.

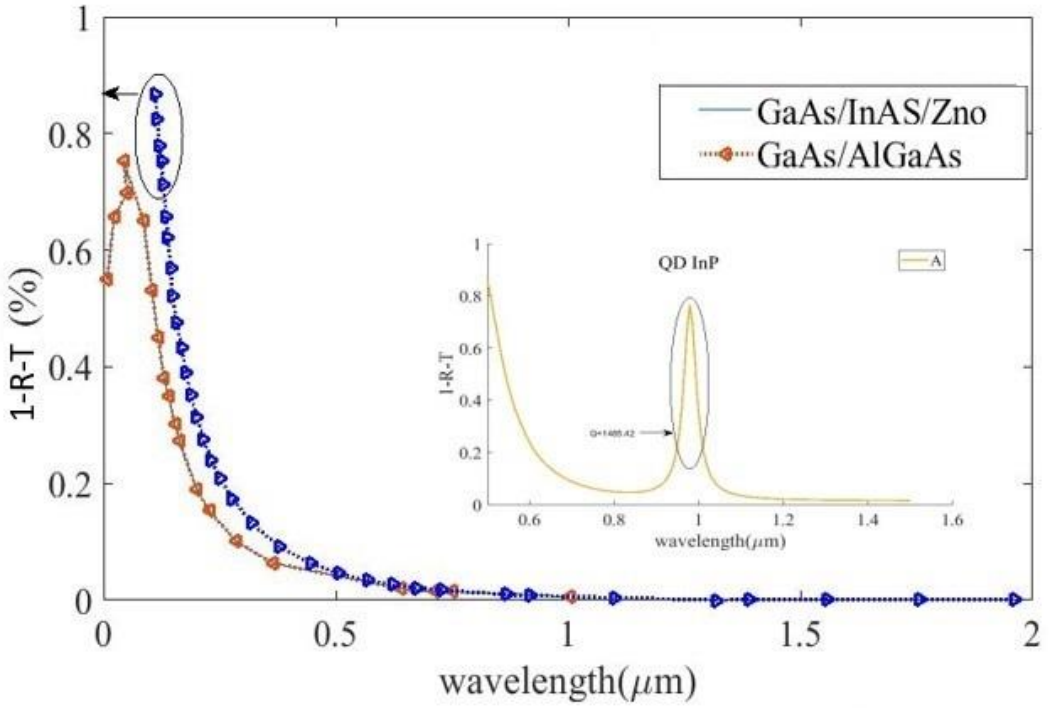

Fig 6: Absorption diagram of active hybrid materials in photonic crystal lasers in wavelength of 1000 nm.

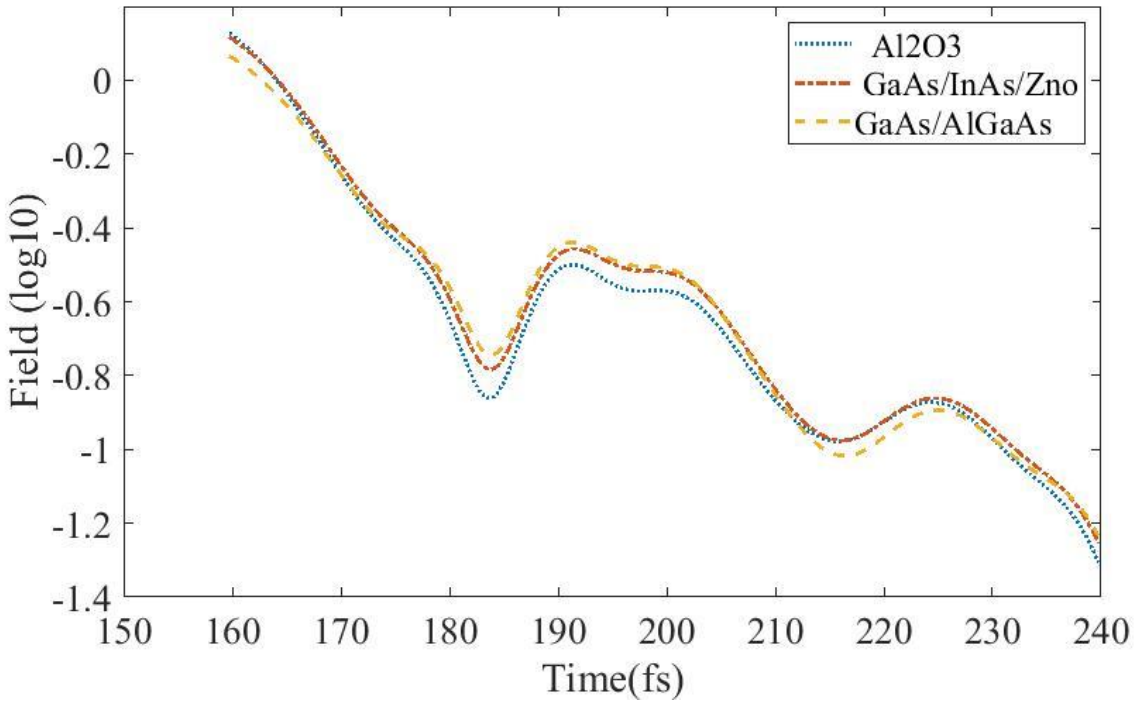

Fig 7: The curve shows the field versus time in the range of 1509 to 240 femtoseconds.

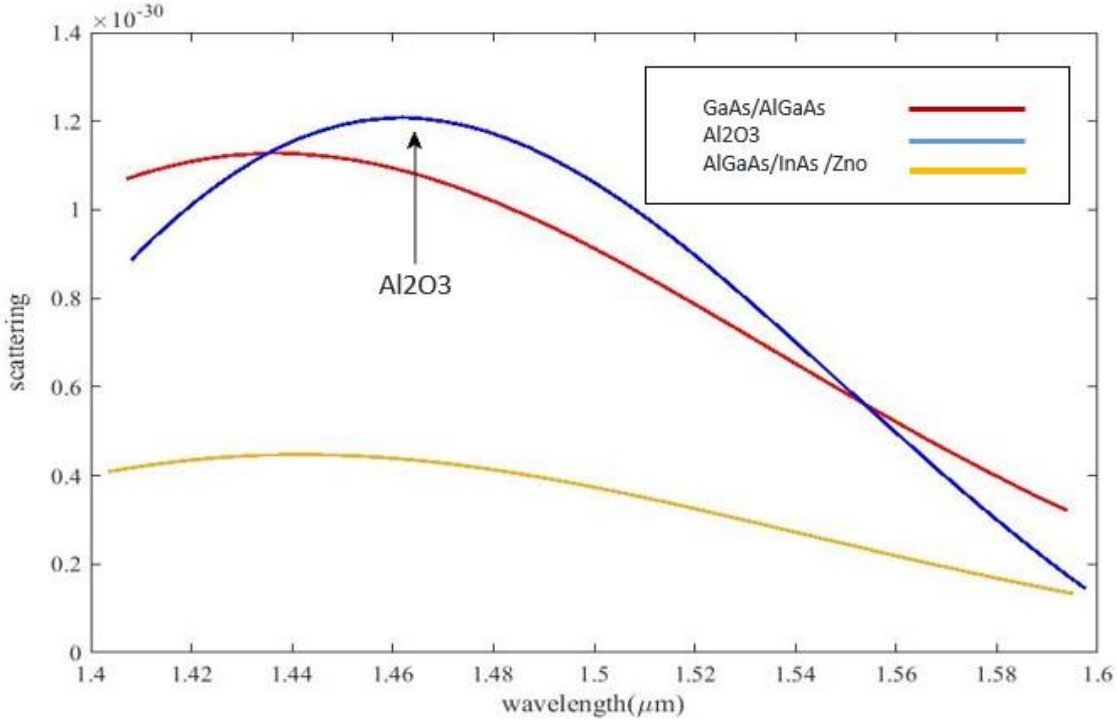

Fig 8: Scattering diagram of hybrid active materials of photonic crystal lasers.

Laser dispersion can depend on the threshold and quality factor of the laser. The dispersion diagram of the active hybrid materials of the photonic crystal laser shows that the combination of aluminum gallium arsenid material and indium arsenic quantum material/zinc oxide shows a 40% lower dispersion compared to the gallium arsenid/aluminum gallium arsenid material. Since the reduction in dispersion is inversely proportional to the quality factor, therefore, the reduction in dispersion increases the quality factor. This feature is effective in reducing the threshold of the photonic crystal laser. The gain and transmission of the active hybrid materials in the photonic crystal laser are examined below.

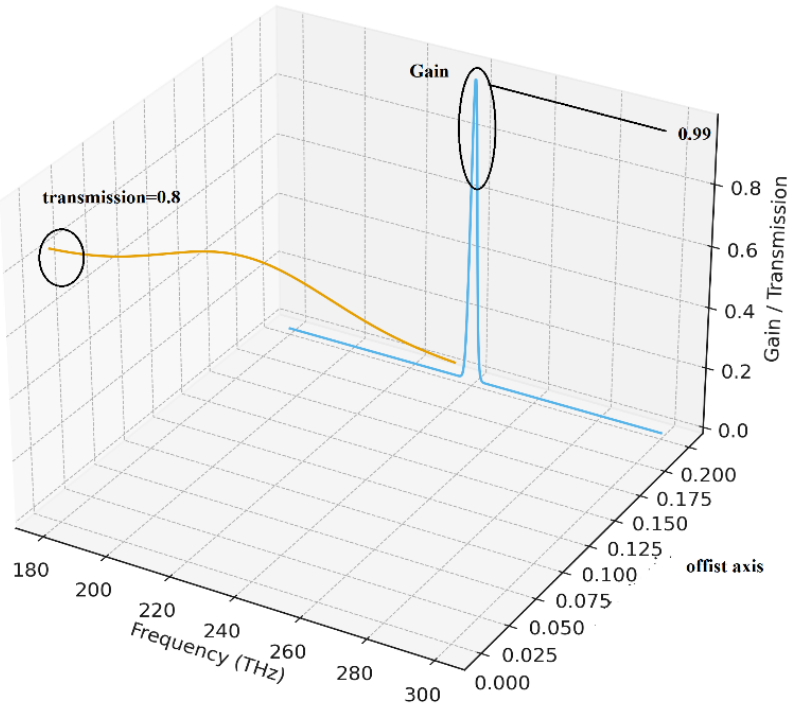

Fig 9: Gain and transmission graph of photonic crystal nanolaser versus frequency in the THz range

The orange curve is the transmission at frequencies from 180 to 260 THz. The transmission value at around 200 THz is 0.8. As the frequency increases, the transmission of the material decreases. This behavior is related to the absorption frequency part of the active material. At lower frequencies, the absorption is low and the transmission is high near the band edge or resonance, and the absorption is high and the transmission is low. For the gain on the right side of the graph, a very sharp peak is seen. The peak value reaches about 0.99 (approximately 1). At a certain frequency, the gain grows suddenly. Then it drops back to near zero. This peak indicates the density of optical states at a frequency of 240 THz. There is a high-quality resonance mode (High-Q mode).

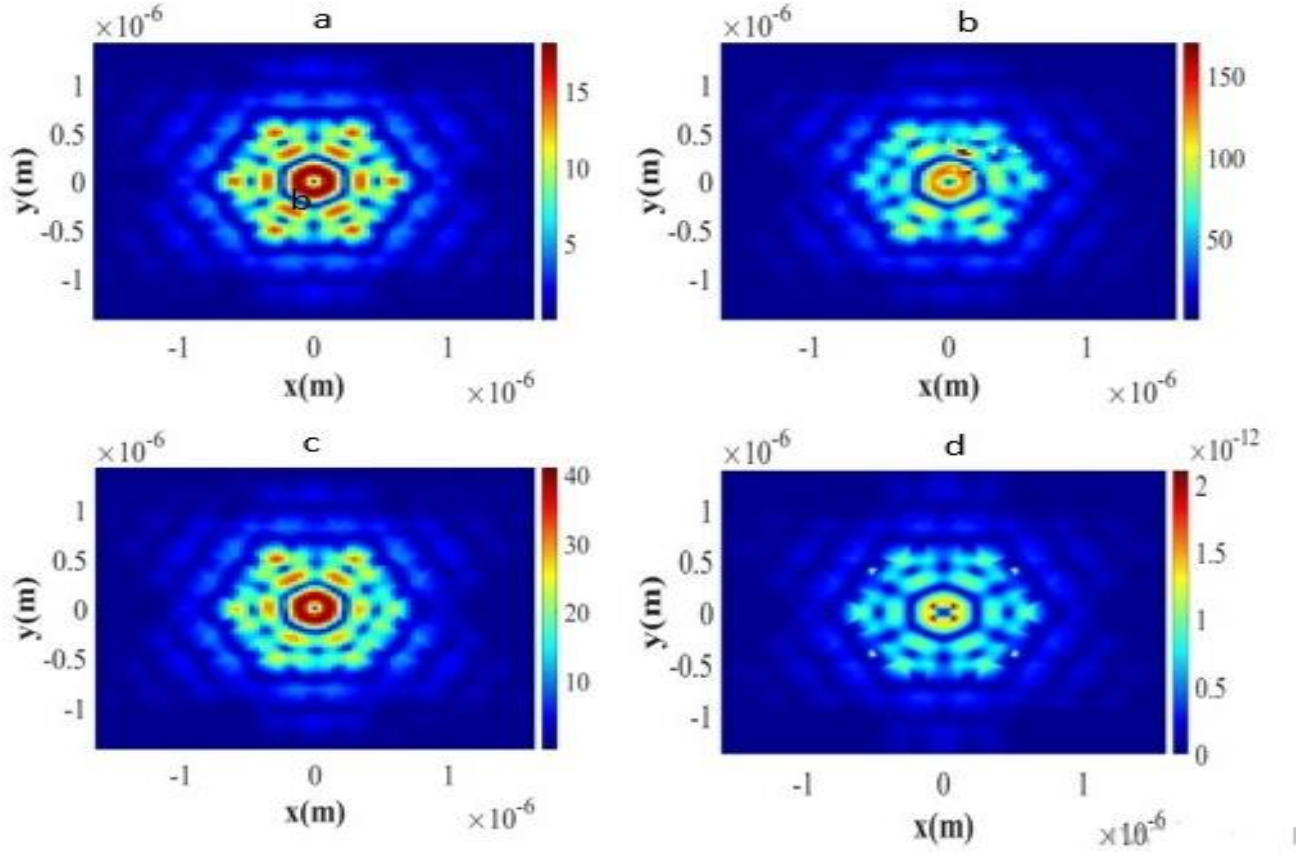

Fig 10: Mode profile of photonic crystals. A) In the state without apodization. B) In apodization. C) Apodization with its effect eliminated at the starting point. D) Apodization with its effect eliminated at the ending point.

Apodization allows the removal of effects that occur near the beginning and/or end of the simulation from the Fourier transform of the monitors. This feature can be useful for filtering out short-term transients that occur when the system is excited by a dipole source and when studying high-Q systems that decay very slowly. Monitor apodization 9a applies a window function to the simulation fields before the monitor performs its Fourier transform of E(t) to obtain E(w). This allows the calculation of E(w) from a portion of the time signal. Start apodization can be used to ignore all transients that occur near the beginning of the simulation.

Figure 10 shows the apodization profile. The magnitude of the electric fields is plotted on the left in Figure 9b. In this image, a superposition of the mode profile and the fields resulting from the transient states is observed. The effect of transients is more pronounced at the source location. The starting apodization is used to get rid of transient states. The green line in the above plots shows the apodization window function used in the simulation for profile 9c. The central time of the window function is set to 1000 femtoseconds to ensure that most of the energy in the cavity is in the available state. Figure 9d shows the final apodization profile, which has no observable effect on the electric field strength from monitor 9a. The difference is that it uses only the final apodization, and the resulting |E|2 plot looks like the monitor plot without any apodization.

V. LASER-BASED OPTIMIZATION OF QUANTUM LOGIC GATES

Recently, nanolasers have been used to control qubits due to their low power, frequency stability, and on-chip integration [21]. Nanolasers are challenging to couple with photonic qubits or other qubits (e.g., atomic or quantum dots) to provide high-quality photons or modulated light; coupling, losses, noise, and fabrication uniformity are complex. Long-term stability, environmental interference, and engineering issues (operating temperature, precise modulation, integration with other quantum components) are still serious obstacles [22]. A Gaussian laser pulse is added as an input (drive) to the quantum circuit. The Gaussian pulse (which has a unitary effect on the qubit) is obtained with a Unitary gate extracted from the pulse model. The Python software qiskit library is used for modeling. The Gaussian laser pulse is equated to a Unitary gate. This gate acts just like a "laser drive" on the qubit. This is the way Qiskit can model "light" or "laser".

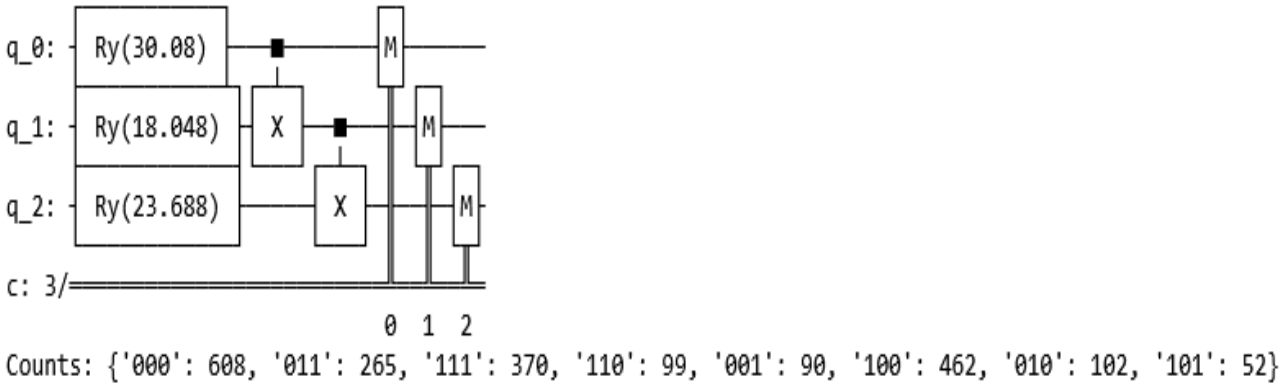

Fig 11: 3-qubit CNOT quantum circuit with a Gaussian laser pulse

A "Gaussian laser pulse" is added as an input (drive) to the quantum circuit. The Gaussian pulse, which has a unitary effect on the qubit, is obtained with a Unitary gate extracted from the pulse model. The Python software qiskit library is used for modeling. The Gaussian laser pulse is equated to a Unitary gate. This gate acts just like a "laser drive" on the qubit. This is how Qiskit can model "light" or "laser". Next, the laser is driven by a 3-qubit cont circuit. Since the use of laser beams in quantum circuits is for angle control and rotation. The schematic of the 3-qubit quantum circuit is shown in Figure 1. The results on angle control and rotation are shown in Figure 12. As can be seen, the Gaussian pulse Q0 has the largest area and therefore the largest angle RY. Q1 has a shorter and shorter pulse, so the rotation angle is smaller. Q2 is located between these two. Pulse area → angle Rotation → The probability of superposition changes in the state $|0\rangle$ and $|1\rangle$. Table I also shows the results for each qubit.

TABLE I

Investigation of the Parameters of the Elevation Area and the Rotation Angle of Each Qubit with the Gaussian Laser Pulse

Qubit	***Omega0***	***sigma***	***wavelength***	***With, Height***
0	1.2	10	Distinct peak, average width	Maximum area → maximum rotation angle
1	0.9	8	Shorter peak and lower	average rotation angle
2	1.05	9	Between Q0 and Q1	medium-high rotation angle

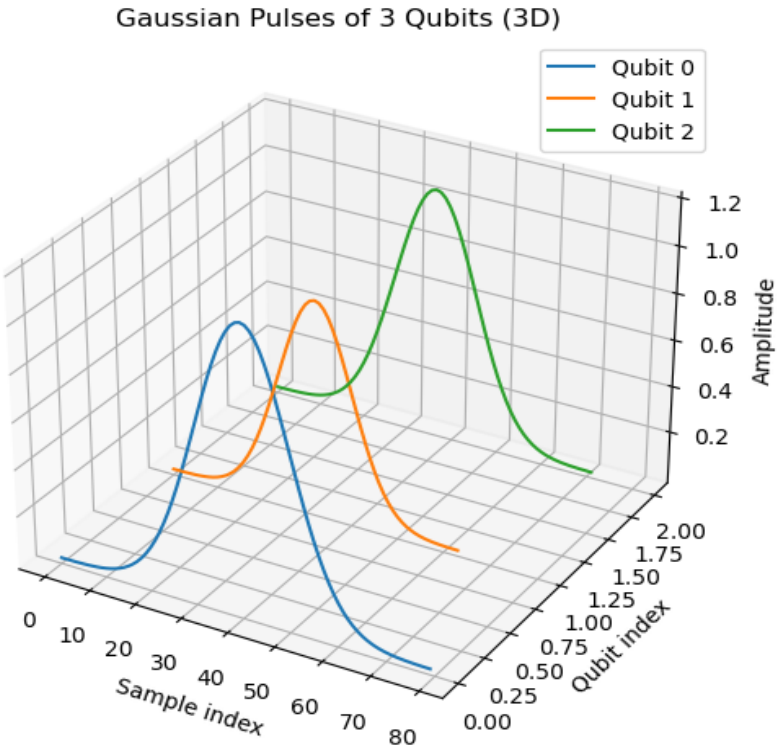

Fig 12: Gaussian wavelet plot for each qubit.

RY(theta) on each qubit Equivalent to applying a Gaussian pulse (by angle θ) causes each qubit to be in the superposition state α|0⟩+β|1⟩\alpha|0\rangle + \beta|1\rangleα|0⟩+β|1⟩.CNOT(0->1) and CNOT(1->2) . These gates cause the qubits to be entangled. Q0 plays the role of control for Q1, and Q1 controls Q2. If Q0 is in the |1⟩ state, Q1 changes, and similarly, Q2 is dependent on Q1.

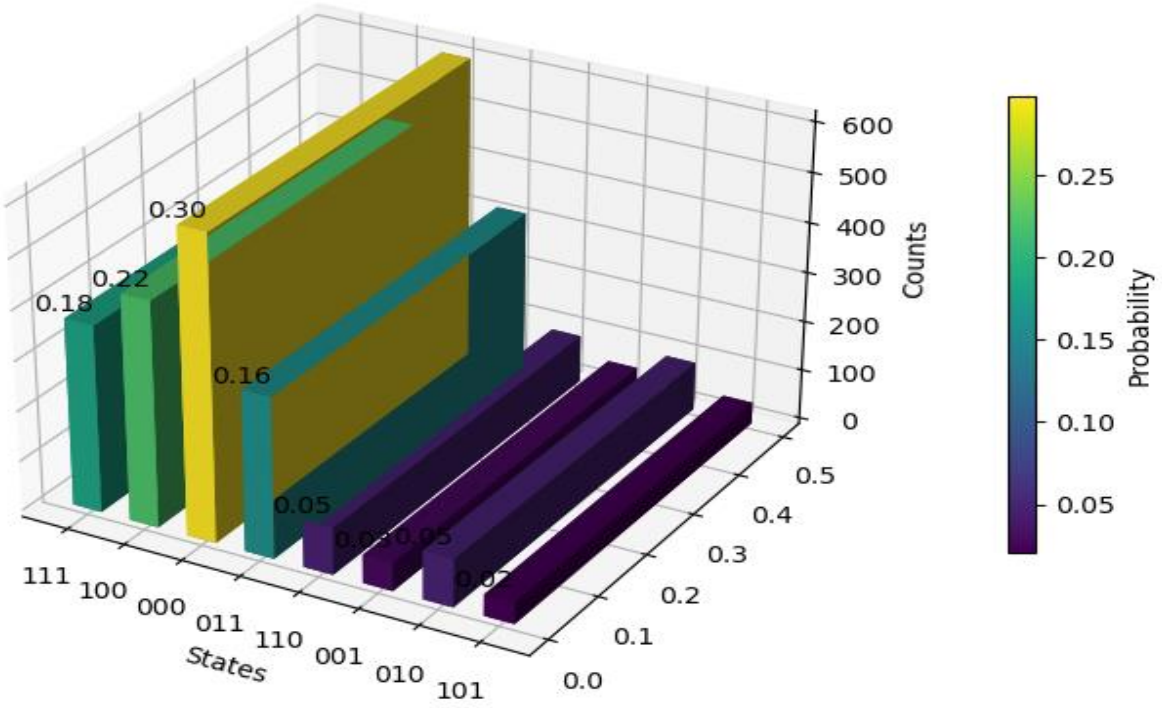

Fig 13: Probability density of qubits correlation with the Gaussian distribution.

In Figure 13 The |000⟩ state has the highest probability (long column + light color) → indicates that most qubits were still close to |0⟩ before CNOT. The |111⟩ state has a significant probability indicates the CNOT chain effect that correlates Q0, Q1, and Q2. Intermediate states such as |001⟩, |010⟩, |101⟩ are less frequently observed. The combination of the RY angle and the CNOT effect makes the distribution non-uniform. The color of the columns is determined by the probability: columns with higher probability are brighter or warmer, and columns with lower probability are darker. The angle θ of each qubit is taken from the area of the Gaussian pulse: $\theta = \Omega 0 * \sigma * \sqrt{(2\pi)}$ Q0, with the largest θ → more likely to change → directly affect Q1 and Q2 via CNOT. Q1 and Q2 have intermediate angles → less likely to superpose → asymmetric probability distribution. Thus, the column |111⟩ indicates the generation of entanglement, since CNOT makes the qubits dependent.

VI. TECHNICAL FEASIBILITY SECTION

The parameter regime required for implementing the proposed protocol is consistent with those already demonstrated in state-of-the-art Rydberg-atom experiments. Typical realizations employ principal quantum numbers in the range, medium densities of , and blockade radii on the order of , depending on the chosen Rydberg state and driving fields. These conditions have been routinely achieved in both cold-atom and thermal-vapor platforms, where strong dipole–dipole interactions and well-resolved EIT features have been reported. Previous studies have also demonstrated stable optical phase control and interaction-mediated nonlinearities at comparable Rydberg excitation densities, confirming that the interaction strengths and coherence times required for our scheme are already experimentally accessible. Taken together, these established capabilities indicate that the proposed approach is feasible with current technology and amenable to near-term experimental realization.

Limitations:

Despite the robustness to decoherence demonstrated in this work, several limitations remain. First, the system retains a degree of sensitivity to photon-loss channels, which may become more pronounced under strong driving conditions or in ultracompact cavity geometries. Second, phase-matching requirements can impose constraints on efficient light–matter coupling, particularly when nonlinear processes or multi-mode interactions are involved. Finally, the scalability of atomic-hole and defect-based gain media is still restricted by fabrication uniformity, spectral inhomogeneity, and integration challenges at the wafer level. Addressing these issues will be essential for transitioning the proposed platform toward large-scale and fully integrated photonic architectures.

Finally, the comparison table is provided as Table II.

TABLE II
The Comparison Table

Reference	Material/Gain Medium	Q-factor	Mode/ Structure	Key innovation/ Feature	Application
[23]	InAs/InP	>100	PhC	High-Q cavity,	**quantum communication and networking**
[24]	Optofluidic	200<	Ring resonator	High sensitivity	**Quantum sensor**
[25]	InAs/InGaAs	-	Quantum dot	Tunable power	**Optical switching devices**
[26]	InAs/GaAs	100<	SOA	Low power	**Logical devies**
This Work	Indium arsenide	227.98	PhC	High-Q cavity, strong light-matter interaction	**Quantum logic gate**
This Work	Aluminium oxide	131.95	PhC	Moderate Q in hybrid gain medium	**Quantum logic gate**

VII.CONCLUSION

In this paper, the hybrid gain medium of quantum dot photonic crystal nanolaser in the increase of the pumping of the var with aluminum oxide, zinc oxide, and gallium arsenide materials has been investigated, and the degree of confinement of the var with a quality factor of 227.89 for the indium arsenic layer and 122.26 has been obtained. Also, increasing the radius variation with a lattice constant rate of 0.37 increases the spontaneous emission, and the linewidth of the modes is limited by the quality factor of the hole. The photonic crystal laser beam is driven into the logic gates of the 3-qubit quantum CNOT circuit, and the results are measured in terms of angle and rotation variations and its probability function for quantum laser application. The Gaussian pulse Q0 has the largest area and therefore the largest RY angle. Q1 has a shorter and shorter pulse, therefore the rotation angle is smaller. Q2 is between these two. Pulse area rotation angle superposition probability changes in the $|0\rangle$ and $|1\rangle$ states.

Funding Declaration
There was no Funding.

DataAvailability
All data is available as a reasonable request from the corresponding authors.

REFERENCES

1.Zhang, Qing, et al. "Halide perovskite semiconductor lasers: materials, cavity design, and low threshold." *Nano Letters* 21.5 (2021): 1903-1914.
2.Jiao, Yuqing, et al. "InP membrane integrated photonics research." *Semiconductor Science and Technology* 36.1 (2020): 013001.
3.Takeda, Koji, et al. "Optical links on silicon photonic chips using ultralow-power consumption photonic-crystal lasers." *Optics Express* 29.16 (2021): 26082-26092.
4.Tomiyasu, Takahiro, et al. "20-Gbit/s direct modulation of GaInAsP/InP membrane distributed-reflector laser with energy cost of less than 100 fJ/bit." *Applied Physics Express* 11.1 (2017): 012704.
5.Aihara, Takuma, et al. "Heterogeneously integrated widely tunable laser using lattice filter and ring resonator on Si photonics platform." *Optics Express* 30.10 (2022): 15820-15829.
6.Wang, Ziye, et al. "Continuous-wave operation of 1550 nm low-threshold triple-lattice photonic-crystal surface-emitting lasers." *Light: Science & Applications* 13.1 (2024): 44.
7.Lee, Tae-Yun, Hansol Lee, and Heonsu Jeon. "Colloidal-quantum-dot nanolaser oscillating at a bound-state-in-the-continuum with planar surface topography for a high Q-factor." *Nanophotonics* 14.10 (2025): 1645-1652.
8.Wang, Yilan, et al. "Large-angle twisted photonic crystal semiconductor nanolasers with ultra-low thresholds operating in the C-band." *arXiv preprint arXiv:2411.14772* (2024).
9.Dimopoulos, Evangelos, et al. "Electrically-Driven Photonic Crystal Lasers with Ultra-low Threshold." *Laser & Photonics Reviews* 16.11 (2022): 2200109.
10.Dhingra, Pankul, et al. "Low-threshold visible InP quantum dot and InGaP quantum well lasers grown by molecular beam epitaxy." *Journal of Applied Physics* 133.10 (2023).
11.Jia, Hui, et al. "Low threshold InAs/InP quantum dot lasers on Si." *2025 IEEE Silicon Photonics Conference (SiPhotonics)*. IEEE, 2025.
12.Wang, Pinyao, et al. "Room temperature CW operation of 1.3 μm quantum dot triple-lattice photonic crystal surface-emitting lasers with buried structure." *Optics Express* 33.13 (2025): 27429-27437.
13.Taghipour, Nima, et al. "Low-threshold, highly stable colloidal quantum dot short-wave infrared laser enabled by suppression of trap-assisted auger recombination." *Advanced Materials* 34.3 (2022): 2107532.

14.Yun, Ling, et al. "Low threshold and high power fiber laser passively mode-locked based on PbSe quantum dots." *IEEE Photonics Technology Letters* 36.4 (2024): 247-250.
15.Tan, Yangzhi, et al. "Low-threshold surface-emitting colloidal quantum-dot circular Bragg laser array." Light: Science & Applications 14.1 (2025): 36.
16.Zhong, Hancheng, et al. "Ultra-low threshold continuous-wave quantum dot mini-BIC lasers." Light: Science & Applications 12.1 (2023): 100.
17.Liu, Jin, et al. "Single self-assembled InAs/GaAs quantum dots in photonic nanostructures: the role of nanofabrication." *Physical review applied* 9.6 (2018): 064019.
18.Shih, Ching-Wen, et al. "Self-Aligned Photonic Defect Microcavity Lasers with Site-Controlled Quantum Dots." Laser & Photonics Reviews 18.7 (2024): 2301242.
19.Yoshida, Masahiro, et al. "High-brightness scalable continuous-wave single-mode photonic-crystal laser." *Nature* 618.7966 (2023): 727-732.
20.Yan, Sai, et al. "Cavity quantum electrodynamics with moiré photonic crystal nanocavity." *Nature Communications* 16.1 (2025): 1-8.
21. Rodt, Sven, and Stephan Reitzenstein. "Integrated nanophotonics for the development of fully functional quantum circuits based on on-demand single-photon emitters. (2021)." *APL Photonics* 6.1.
22.Shang, Chen, et al. "Perspectives on advances in quantum dot lasers and integration with Si photonic integrated circuits." *ACS photonics* 8.9 (2021): 2555-2566.
23. Phillips, C.L., Brash, A.J., Godsland, M., Martin, N.J., Foster, A., Tomlinson, A., Dost, R., Babazadeh, N., Sala, E.M., Wilson, L. and Heffernan, J., 2024. Purcell-enhanced single photons at telecom wavelengths from a quantum dot in a photonic crystal cavity. Scientific Reports, 14(1), p.4450.
24. Mozaffari, M.H. and Farmani, A., 2019. On-chip single-mode optofluidic microresonator dye laser sensor. *IEEE sensors Journal*, *20*(7), pp.3556-3563.
25. Heydari, M., Zali, A.R., Gildeh, R.E. and Farmani, A., 2022. Fully Integrated, 80 GHz Bandwidth, 1.3μ m InAs/InGaAs CW-PW Quantum Dot Passively Colliding-Pulse Mode-Locked (CPM) Lasers for IR Sensing Application. *IEEE sensors journal*, *22*(7), pp.6528-6535.
26. Farmani, A., Farhang, M. and Sheikhi, M.H., 2017. High performance polarization-independent quantum dot semiconductor optical amplifier with 22 dB fiber to fiber gain using mode propagation tuning without additional polarization controller. *Optics & Laser Technology*, *93*, pp.127-132.